

Cite this article as: Wang Wenqin, Chen Jigen, Yan Xiaosong, et al. Microstructure and Properties of SiCp/Al Composite Materials Fabricated via Powder Packed Resistance Additive Manufacturing[J]. Rare Metal Materials and Engineering, 2024, 53(11): 3035-3045. DOI: 10.12442/j.issn.1002-185X.20240020.

ARTICLE

Microstructure and Properties of SiCp/Al Composite Materials Fabricated via Powder Packed Resistance Additive Manufacturing

Wang Wenqin¹, Chen Jigen¹, Yan Xiaosong³, Han Zhaoxian⁴, Lin Gang², Chen Jie²

¹ School of Mechanical and Electrical Engineering, Nanchang University, Nanchang 330031, China; ² Institute of Special Equipment Inspection and Research, Jiangxi General Institute of Testing and Certification, Nanchang 330029, China; ³ Jiangxi Sinohexaco Helicopter Co., Ltd, Jingdezhen 333032, China; ⁴ Jiangxi Haoyu Heavy Industry Co., Ltd, Ruijin 341000, China

Abstract: SiC particle (SiCp)/Al composite materials were fabricated via powder packed resistance seam welding additive manufacturing. The influence of welding speed on microstructure and mechanical properties of the specimen was investigated, elucidating the formation and fracture mechanism of single-pass multi-layer deposition. The results demonstrate that a dense internal structure of the specimen characterized by uniformly dispersed SiCp embedded within the Al matrix is formed. However, particle agglomeration and porosity defects are observed. The porosity increases with the increase in welding speed, and the microstructure of the RSAM-24 specimen has the highest density, characterized by a density of 2.706 g/cm³ and a porosity of 1.672%. The mechanical properties of the specimens decrease as the welding speed increases. Optimal mechanical properties are obtained when the welding speed is set as 24 cm/min. Specifically, the average hardness, tensile strength and elongation values are 463.736 MPa, 52.16 MPa and 2.2%, respectively. The tensile specimens predominantly exhibit fracture along the interlayer bonding interface and the interface between the Al matrix and SiC particles, and the damage mode is ductile fracture.

Key words: additive manufacturing; resistance seam welding; SiCp/Al; hardness; welding speed

Aluminum (Al) alloys are widely acknowledged and highly focused due to their exceptional properties, encompassing superior specific strength, remarkable corrosion resistance and suitability for diverse machining processes^[1-3]. Recently, Al alloys processed by laser powder bed fusion additive manufacturing have shown strong and ductile properties^[4]. The utilization of Al alloys, however, is restricted by certain inherent drawbacks, such as low hardness, insufficient wear resistance, subpar plasticity and a relatively low melting point^[5]. The use of ceramic reinforced metal matrix composites represents an efficacious approach for enhancing these properties^[6-9]. These composite materials possess the advantageous such as high hardness and good wear resistance derived from the ceramic phase^[10-13] while retaining the desirable characteristics of the original Al matrix materials^[14-15]. Silicon carbide (SiC) has gained significant

adoption among the wide range of available ceramic particles due to its cost-effectiveness and exceptional performance^[16-19].

Xiao et al^[20] conducted a comprehensive investigation on the tensile properties of SiC particle (SiCp)/Al composites using the powder metallurgy approach. The results shed light on the influence of volume fraction and SiC particle size on tensile properties. The powder metallurgy allows flexible control of the amount of reinforcement added and convenient regulation of the volume fraction. However, it is worth noting that the composites often exhibit irregular internal organization and a significant degree of porosity, leading to suboptimal mechanical properties. Laser additive technique^[21] has also been employed for the fabrication of SiCp/Al composites^[22-23]. However, due to the higher laser absorption capacity of Si (78%) compared to that of Al (7%), SiCp is susceptible to ablation during the process, resulting in a

Received date: January 12, 2024

Foundation item: National Natural Science Foundation of China (52205375); Major Discipline Academic and Technical Leaders Training Program of Jiangxi Province (20204BCJ23003); Jiangxi Provincial Natural Science Foundation (20224BAB214010, 20232BAB204049, jxsq2019201118)

Corresponding author: Chen Jie, Ph. D., Associate Professor, Institute of Special Equipment Inspection and Research, Jiangxi General Institute of Testing and Certification, Nanchang 330029, P. R. China, Tel: 0086-791-88176280, E-mail: ncuchenjie@126.com

Copyright © 2024, Northwest Institute for Nonferrous Metal Research. Published by Science Press. All rights reserved.

reduction in content as well as alterations in particle distribution and morphology^[24]. Furthermore, under conditions of elevated heat input, SiC readily reacts with molten Al, leading to the formation of the brittle Al_4C_3 phase, which significantly degrades the mechanical properties of the material^[25]. Therefore, the use of additive manufacturing method with low energy density and balanced heat input is essential for the preparation of SiCp/Al composites.

Resistance seam welding is a technique for joining materials together that involves positioning the workpiece between two electrode wheels, applying pressure by rolling the electrode wheels, and applying energy to create Joule heat to encourage heat generation and local melting of the base material to create a continuous weld^[26-27]. Resistance fusion cladding technique, which has been used to prepare thicker coatings by pre-positioning the powder for welding^[28-29] with low heat input during the preparation process, is evolved from resistance seam welding as a method of joining materials. The prepared coatings exhibit a dense structure with excellent mechanical properties. Based on this, the additive manufacturing technique of resistance seam welding is proposed. In comparison to other additive manufacturing techniques^[30], resistance seam welding features low and uniform energy input, without generating harmful intermetallic compounds.

In this study, a novel additive manufacturing technique of low-energy resistance seam welding based on composite powder stacking was proposed for the fabrication of SiCp/Al composites, which takes advantage of the unique material properties of both SiC and Al particles and combines the principle of the current self-selected low-resistance path to improve the retention rate of SiC particles. 10vol% SiCp/Al composites were prepared and the influence of the welding speed on the microstructure and mechanical properties was

discussed. Additionally, the formation and fracture mechanism of the single-pass multi-layer deposition layer were revealed.

1 Experiment

1.1 Materials

The research object chosen for this study was Al 1060 and SiC powders. The chemical composition of Al 1060 powder is shown in Table 1. The scanning electron microscope (SEM) image in Fig. 1a depicts the Al 1060 powder, which exhibits a relatively rough surface morphology with poor spheroidization. The majority of powder particles appear as dumbbell or ellipsoid shapes, while a minority exhibits irregular shapes. The particle size distribution is illustrated in Fig. 1b, with the predominant particle size of 200–500 μm . Fig. 1c depicts that the SiC powder is an irregular non-spherical particle, and the particle size is in the range of 8–24 μm (Fig. 1d).

1.2 Preparation of specimens

The SiCp/Al composites were prepared by blending Al 1060 and SiC powders in a volumetric ratio of 9:1. SUS 304 stainless steel (50 mm×50 mm×5.8 mm) was used as the substrate, which was initially treated with 180# emery paper to eliminate oxides and then ultrasonically cleaned in acetone. Al 1060 powder with a thickness of 1.5 mm was preset on the treated substrate surface. Specifically, SUS 304 stainless steel foil with a thickness of 100 μm was used on the surface of each pre-deposited layer to protect the electrodes, and the stainless steel foil was removed from the surface after welding slice. The test was conducted in an open atmosphere. All

Table 1 Chemical composition of Al 1060 powder (wt%)

| Fe | Si | Cu | Mg | Mn | Al |
|------|------|------|------|------|------|
| 0.25 | 0.35 | 0.05 | 0.03 | 0.03 | Bal. |

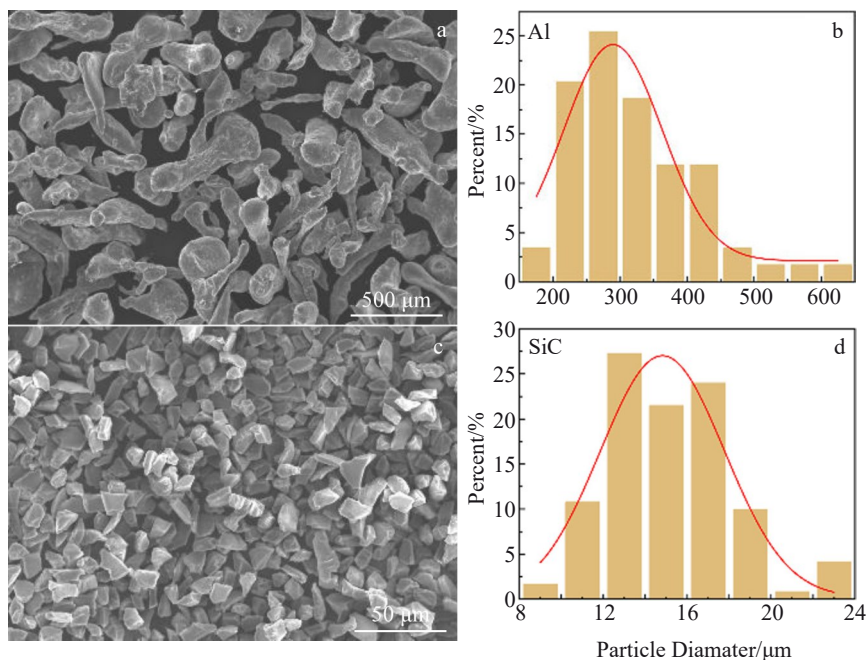


Fig. 1 SEM images (a, c) and particle size distributions (b, d) of Al 1060 powder (a–b) and SiC powder (b–d)

specimens were fabricated via the FN-160 intermediate frequency seam welder (Pengri, Changzhou, China) which consisted mainly of the electrode wheel and the lower copper electrode platform. Fig. 2 shows the deposition process of resistance additive manufacturing. The welding process parameters are listed in Table 2. For comparison, the specimens were deposited at welding speeds of 24, 48 and 72 cm/min, named as RSAM-24, RSAM-48 and RSAM-72, respectively. The size of the specimens was basically the same under macro conditions, the length was 70 mm, the width was about 7 mm, and the thickness of RSAM-24, RSAM-48 and RSAM-72 specimens was 9.34, 9.23 and 9.41 mm, respectively.

1.3 Characterization of materials

The cross-section microstructure of each specimen was observed by a sophisticated depth-of-field optical microscope (OM, Keyence VHX6000, Japan). To identify the phases in the specimens, micro-X-ray diffractometer (XRD, D8 ADVANCE, BRUKER, Germany) analysis was conducted with Cu-K α radiation at 50 kV and a tube current of 45 mA. The specimens were scanned in the 2θ range of 20° – 100° with step angle of 0.085° and scan speed of $0.1^\circ/s$. The phase composition was analyzed by Jade 6.0 software. Additionally, the phase composition at the interface was analyzed by transmission electron microscope (TEM, FEI Talos F200X, USA). The microstructure of powders, cross-sections of specimens, and morphology of tensile fracture were observed by SEM (FEI Quanta 200FEG, USA) equipped with energy-dispersive spectrometer (EDS).

The hardness of the specimens was measured by a microhardness tester (TMHV-1000Z, Jinan, China) under a load of 0.98 N with a dwell time of 10 s. The nanohardness and elastic modulus of the specimens were investigated by nanohardness tester (HM 2000, Fischerscope, Germany). The instrument was equipped with a Berkovich four-pronged conical indenter with maximum indentation load of 50 mN, loading time of 20 s and longitudinal and transverse spacing of 10 μm . The tensile properties of the specimens were tested by an in-situ bidirectional tensile tester (IBTC-2000, Tianjin, China) at room temperature, and the strain rate was set as 10^{-3} s^{-1} .

2 Results and Discussion

2.1 Microstructure characterization

Fig. 3 shows the xoz cross section of the specimen at various speeds, which is perpendicular to the welding direction. The macroscopic morphology shows a trapezoidal shape with narrow top and wide bottom, as shown in Fig. 3a, 3d and 3g. Fig. 3b–3c, 3e–3f, 3h–3i are the enlarged images of the specimens. It is worth noting that obvious bonding interfaces are observed in all samples. SiCp is distributed on the matrix of Al 1060, and there is agglomeration phenomenon. In addition, a few pores and other defects in the specimen are observed^[31].

Fig. 4 shows SEM images and corresponding EDS element mappings of specimens. The Si element in the RSAM-72 specimen is surrounded by Al, indicating the presence of agglomerated SiCp on the surface of unmelted or partially

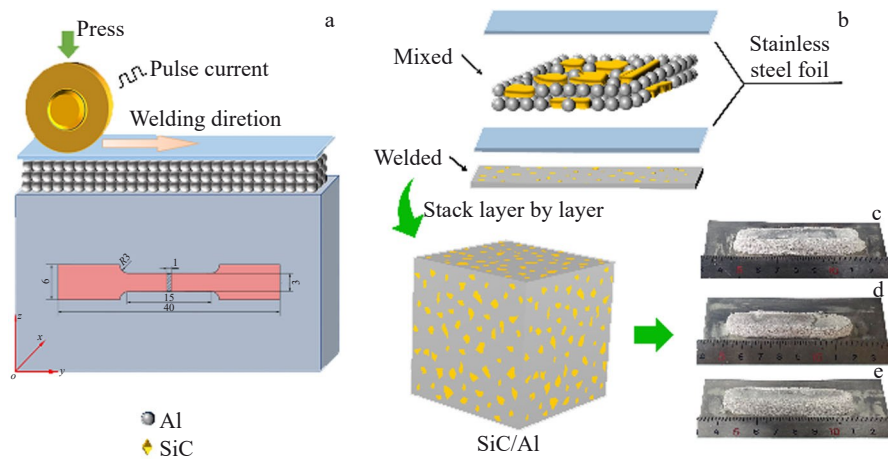


Fig. 2 Schematic diagrams of resistive additive manufacturing and dimensions of tensile specimen (a) and physical drawing of molding process (b); macro appearances of RSAM-24 (c), RSAM-48 (d), and RSAM-72 (e)

melted Al 1060. These particles retain their original form after cooling and solidification. Similarly, as depicted in Fig. 4d–4e, this phenomenon is observed in both xoy and $yo z$ cross sections of RSAM-72 specimen. However, decrease in welding speed results in a diminished entrapment phenomenon, which is not observed in the RSAM-24 specimen.

A few air pores are observed in the RSAM-24, RSAM-48 and RSAM-72 specimens, and the porosity can be quantified

Table 2 Welding process parameters

| Welding current/kA | Welding speed/cm·min ⁻¹ | Welding pressure/MPa |
|--------------------|------------------------------------|----------------------|
| 5 | 24 | 0.4 |
| | 48 | |
| | 72 | |

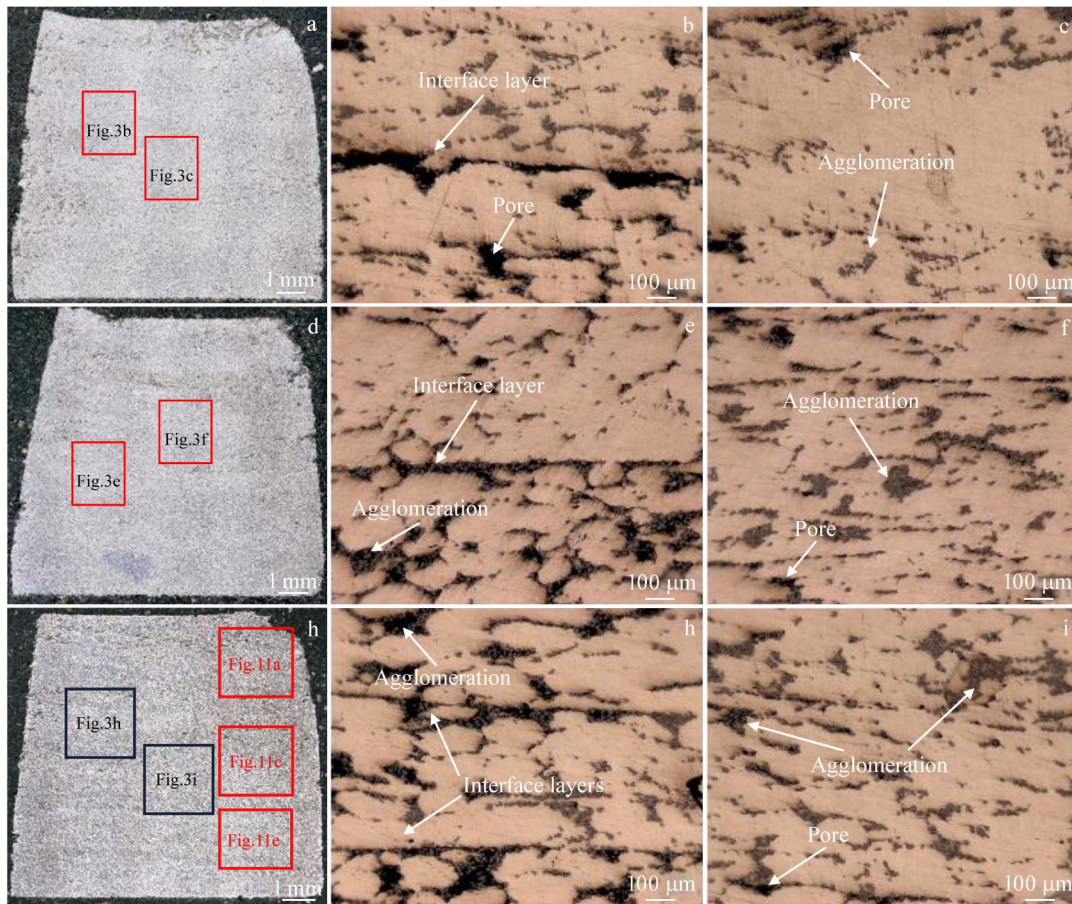


Fig.3 Macroscopic morphologies (a, d, g) and corresponding enlarged images (b–c, e–f, h–i) of xoz sections of specimens with different welding speeds: (a–c) RSAM-24, (d–f) RSAM-48, and (g–i) RSAM-72

by Eq.(1)^[32]:

$$\text{Porosity} = \left[\frac{\rho_{\text{th}} - \rho_{\text{exp}}}{\rho_{\text{th}} - \rho_{\text{a}}} \right] \times 100\% \quad (1)$$

where ρ_{exp} is the experimental density, which is calculated by Archimedes' drainage method; ρ_{a} is the air density; ρ_{th} is the theoretical density calculated by Eq.(2).

$$\rho_{\text{th}} = V_{\text{Al}}\rho_{\text{Al}} + V_{\text{SiC}}\rho_{\text{SiC}} \quad (2)$$

where V_{Al} and V_{SiC} are the volume fractions of Al and SiC, respectively; ρ_{Al} and ρ_{SiC} are the theoretical densities of Al 1060 and SiC, respectively.

The results are presented in Table 3, revealing an inverse correlation between welding speed and specimen density as well as an positive relationship between welding speed and porosity. The porosity within the specimen is attributed to two primary factors. Firstly, the agglomerated SiCp hinders the complete filling of molten Al in the interparticle gaps, as depicted in Fig. 5a–5c. Secondly, irregular shapes of SiCp coupled with low temperature hinder effective wetting and spreading of molten Al on the surfaces, leading to pores between Al and SiCp (Fig. 5d). Consequently, the porosity of SiCp/Al resistive additive manufactured composites is significantly higher than that of Al 1060.

The proportion of melted Al 1060 particles and the availability of molten Al to fill voids between SiCp increase with slowing welding speed. Meanwhile, the slower welding

speed also leads to a slower temperature drop, allowing for a longer duration of molten state for Al, which enhances void filling. Consequently, lower numbers of pores in the first category are observed at slower welding speed. Additionally, increased electrode pressure resulting from slower welding speed facilitates the spreading of molten Al on SiCp surfaces, leading to a decrease in the number of pores in the second category. This explains the increase in porosity with increasing the welding speed for specimens.

Relevant interfacial reactions in metal matrix composites contribute to the enhancement of the interfacial bonding strength between the reinforcement and the matrix. The predominant interfacial reaction in the SiCp/Al system is $3\text{SiC} + 4\text{Al} \rightarrow \text{Al}_4\text{C}_3 + 3\text{Si}$, which results in the formation of Al_4C_3 , a brittle phase that adversely affects material properties^[33]. Fig.6 shows XRD patterns of powder raw material and the specimens fabricated at different welding speeds. It reveals that both the specimen and powder exclusively exhibit Al and SiC phases, thereby indicating the absence of any discernible interfacial reaction between Al and SiC which leads to the formation of deleterious Al_4C_3 .

Based on thermodynamic calculation of Gibbs free energy, it has been determined that the interfacial reaction occurs within the temperature range of 923–1620 K^[34]. To investigate the interfacial bonding and possible reactions, the RSAM-24

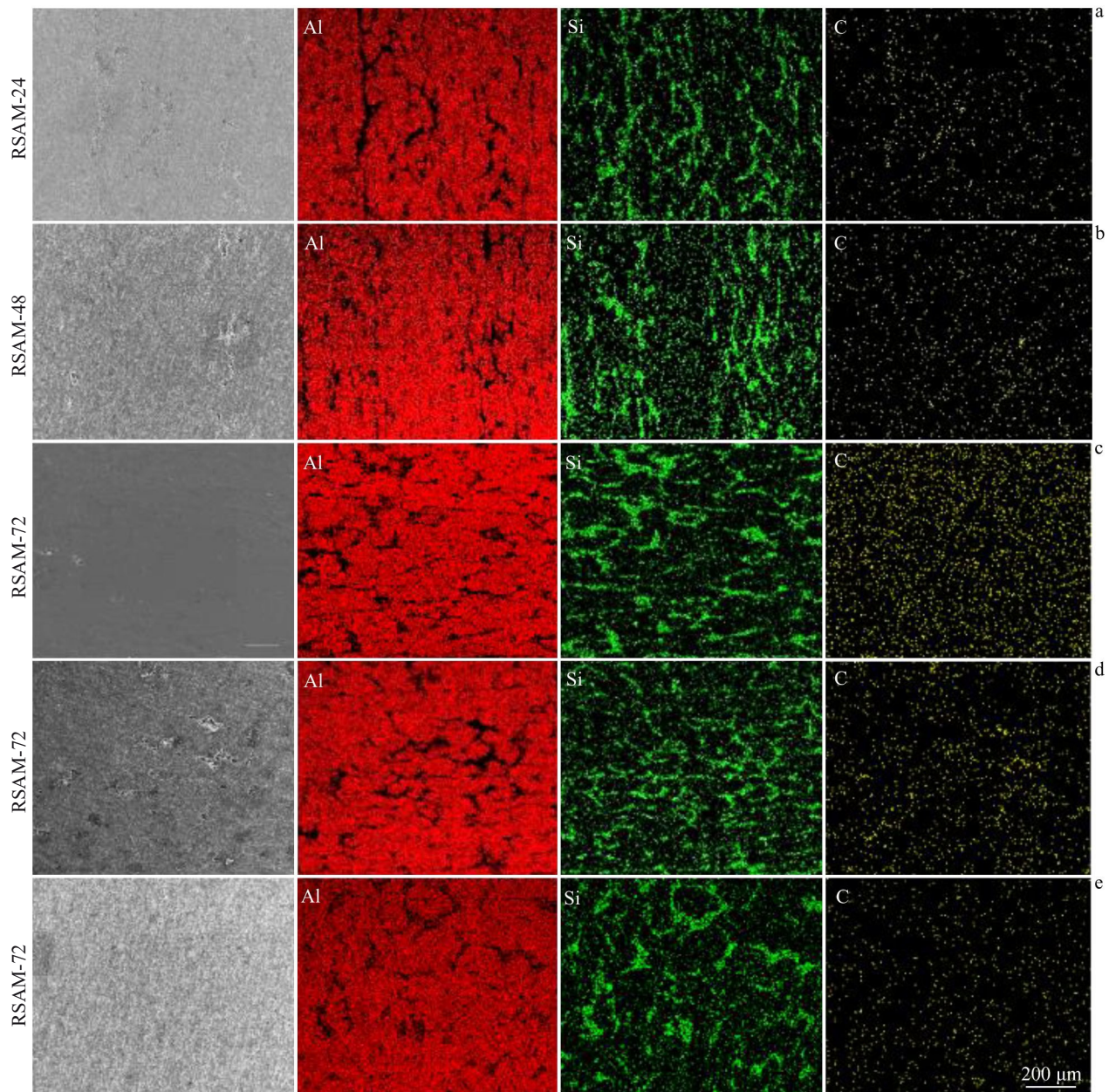


Fig.4 SEM images and corresponding EDS element mappings of different cross sections of specimens: (a–c) *xoz*, (d) *xoy*, and (e) *yoz*

Table 3 Calculated density and porosity of specimens

| Specimen | Theoretical density/ $\text{g}\cdot\text{cm}^{-3}$ | Experimental density/ $\text{g}\cdot\text{cm}^{-3}$ | Porosity/% |
|----------|--|---|------------|
| RSAM-24 | | 2.706 | 1.672 |
| RSAM-48 | 2.752 | 2.700 | 1.877 |
| RSAM-72 | | 2.694 | 2.116 |

specimen, characterized by the lowest welding speed and the highest heat input, was selected for TEM analysis. As shown in Fig. 7a, TEM bright field image reveals a well-established interfacial bonding between the SiCp and the matrix. The interfacial bonding appears smooth and clean, ruling out the formation of needle-like Al_4C_3 phase and indicating that there is no significant interfacial reaction between Al and SiC

during the experimental process. Furthermore, TEM observations demonstrate that the highest dislocation density occurs within individual grains at the interface, attributing to the inhomogeneous plastic strain of the matrix material when deformed around the rigid SiC grains. Fig. 7b–7c present the selective area electron diffraction (SAED) pattern obtained for SiC and Al regions, with crystallographic zone axes of [100] and [011], respectively.

2.2 Formation mechanism

The primary heat input in resistance additive manufacturing is the radial Joule heat generated by the current passing through the point contact between the aluminum powders. It is assumed that all the heat is converted to an increase in the temperature of the materials. The principle simplification is shown in Fig. 8a. The two horizontally adjacent powders

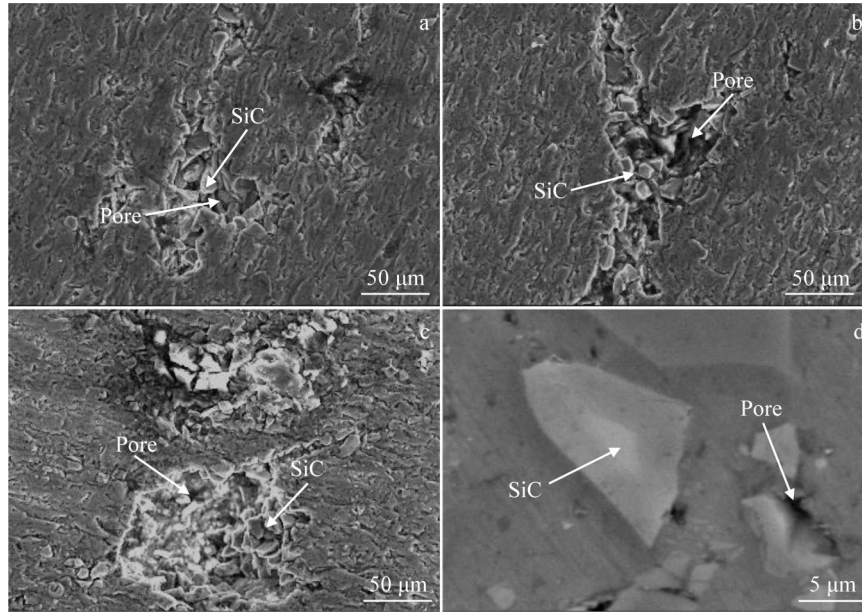


Fig.5 SEM images of defects in RSAM-24 (a), RSAM-48 (b), and RSAM-72 (c-d)

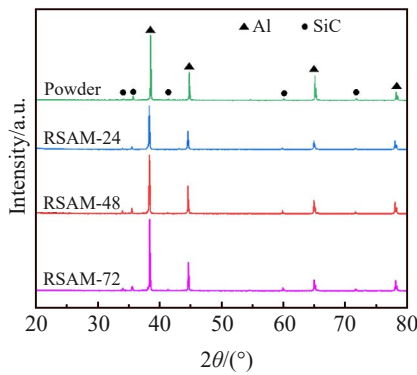


Fig.6 XRD patterns of powder raw material and RSAM-24, RSAM-48 and RSAM-72 specimens

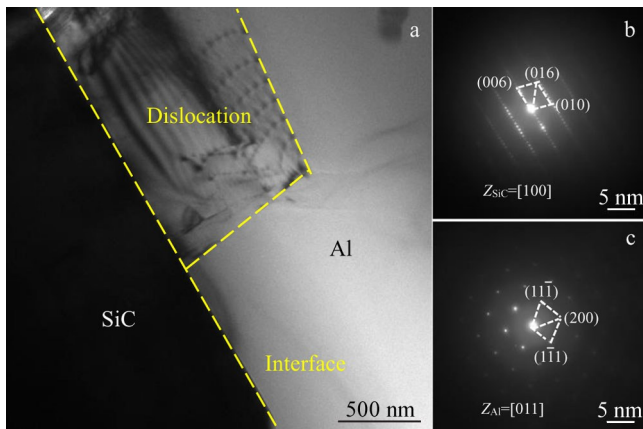


Fig.7 TEM bright field image of RSAM-24 specimen (a) and SAED patterns of SiC (b) and Al (c)

belong to the parallel circuit, as shown in Fig.8b. Therefore, the relationship between Joule thermal effect and powder

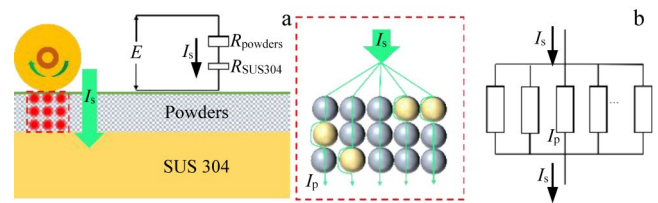


Fig.8 Schematic diagrams of heat input (a) and equivalent circuit (b) of single layer in resistance seam welding

temperature can be expressed as follows:

$$\Delta T = \frac{16}{\pi^2} \frac{I_p x^2 \rho \Delta t}{C_v \rho_m [r^2 - (r-x)^2]^2} \quad (3)$$

where Δt is one quarter of the alternating current cycle; C_v is the heat capacity; r is the radius of the powder particle; ρ is the resistivity; ρ_m is the powder density; I_p is the radial current; x is the distance to the contact area. Table 4 shows the parameters for calculating the instantaneous temperature. When x is less than or equal to $5 \mu\text{m}$, the contact resistance is very high, resulting in an instantaneous temperature increase more than 2000 K, which is significantly higher than the melting point of powders. When x exceeds $5 \mu\text{m}$, the instantaneous temperature increment is only 30 K, suggesting that the particles within the powder are minimally impacted by the instantaneous Joule heat effect. Consequently, the current passing through the powder generates a Joule thermal

Table 4 Parameters for calculation of the instantaneous temperature of Al 1060 powder

| $\rho_m / \text{g} \cdot \text{cm}^{-3}$ | $\rho / \times 10^{-6} \Omega \cdot \text{m}$ | $C_v / \times 10^3 \text{ J} \cdot (\text{kg} \cdot ^\circ\text{C})^{-1}$ | $\Delta t / \text{s}$ | $r / \mu\text{m}$ | I_s / kA | I_p / A |
|--|---|---|-----------------------|-------------------|-------------------|------------------|
| 2.71 | 2.85 | 0.88 | 0.02 | 65 | 5 | 1 |

effect, leading to localized high temperatures and causing the powder to melt and to consolidate under the influence of electrode pressure.

During the welding process, although the powder on both sides of the electrode wheel does not directly contact the wheel, there is a shunt effect (I_p) due to the contact conductivity among the powder, the stainless steel foil and the powder particles, generating a radial current as depicted in Fig. 9a. Consequently, the shunt current gives rise to Joule heating, leading to the melting of the powder on both sides of the electrode wheel. Typically, the width of the single pathway exceeds that of the electrode wheel. However, due to the absence of radial electrode pressure on both sides and the low shunt current density, there is a reduced Joule heat, resulting in increased internal defects. These internal defects contribute to resistance increase, resulting in a lower R_m (middle resistance) compared to R_b (two sides resistance). The continuous welding process induces a preferential current flow towards the region with lower resistance, leading to a reduction in the width of the weld path, as shown in Fig. 9b. Consequently, the xoz cross section of the specimen exhibits a trapezoidal shape. Moreover, the conduction time of current will be influenced by the welding speed, with a narrower weld path resulting from higher welding speeds.

The schematic diagram in Fig. 9c illustrates the forming process of SiCp/Al composites. During the welding process, in accordance with the principle of following paths with lower resistance, predominant current flow is observed along the Al 1060 particles. The high contact resistance between Al 1060 particles is induced by the pulse current, resulting in a substantial generation of instantaneous Joule heat, which subsequently leads to partial melting of the particles. The molten Al infiltrates the voids between SiC powder particles

through electrode pressure and capillary action, resulting in a metallurgical bonding upon solidification. The absence of interfacial reaction can be attributed to the low heat input process. The SiCp does not exhibit any Joule heating effect, whereas the transient Joule heat generated between the Al 1060 particles primarily contributes to the melting of the Al particles. This transient heat can only raise the temperature of the SiCp by thermal conduction. The heat transferred to the SiCp is possibly insufficient to reach the reaction temperature. Additionally, the cooling rate is relatively rapid, resulting in the solidification of molten Al before any reaction occurs within a short period of time.

2.3 Hardness analysis

The results of the Vickers hardness analysis are shown in Fig. 10. Fig. 10a illustrates the direction of hardness measurement, with a single data point recorded every 100 μm interval. The hardness distribution exhibits significant fluctuations along the $oz-xoz$ direction for the specimens (Fig. 10d). It can be attributed to the uniform distribution of SiC on the Al substrate. Considering that the hardness of SiC is significantly higher than that of Al, the areas affected by SiCp exhibit notably elevated hardness values. Average hardness of RSAM-24, RSAM-48 and RSAM-72, along $oz-xoz$ direction is 463.736, 410.130 and 381.416 MPa, respectively. The average hardness decreases with the increase in welding speed, which is related to the porosity of the specimen (Fig. 10b). Fig. 10c shows the hardness distribution of RSAM-72 along the $oz-yoz$, $ox-xoy$ and $oy-xoy$ directions. The hardness of the two sides along the $ox-xoy$ direction is significantly lower than that of the intermediate Al matrix, which is consistent with the previous indication that there are a higher density of defects in these regions.

The nanoindentation investigation was conducted to explore

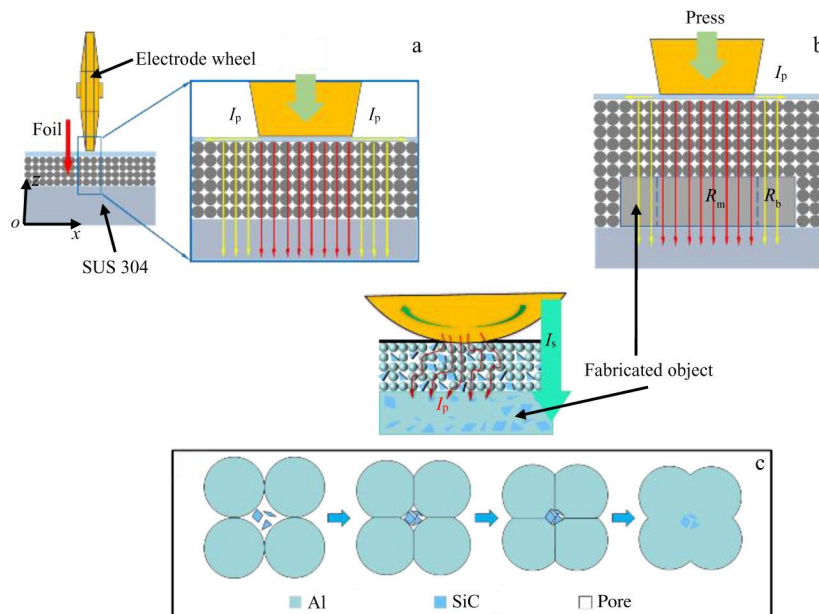


Fig.9 Schematic diagrams of powder diversion during resistance seam welding: (a) single layer, (b) multi-layer, and (c) resistive additive SiCp/Al composites

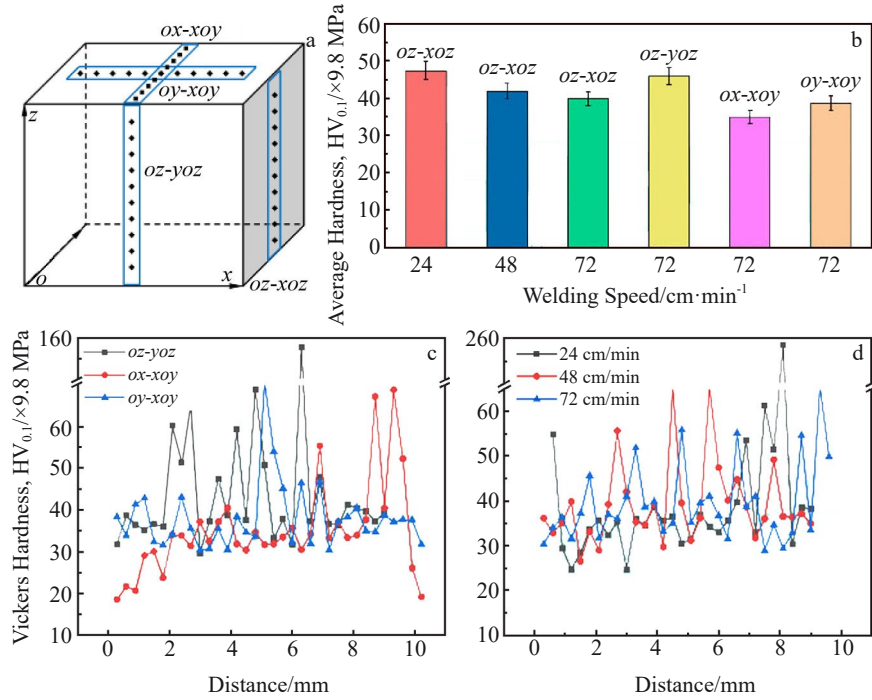


Fig.10 Schematic of hardness measurement direction (a) and average hardness (b); Vickers hardness distribution of RSAM-72 along different directions (c); Vickers hardness distribution of different specimens along $oz-xoz$ direction (d)

the influence of microstructure on mechanical behavior. Fig.11 presents the nanohardness distribution of the RSAM-72 specimen in the corresponding region as depicted in Fig.3g. There is an evident correlation between mechanical properties and microstructure. The areas where SiC is distributed exhibit high nanohardness values, reaching up to 17.44 GPa. Moreover, the presence of SiCp simultaneously enhances the local nanohardness of the matrix, resulting in a higher

hardness of the Al matrix surrounding these particles compared to other regions.

2.4 Tensile strength analysis

The stress-strain curves of the specimens are presented in Fig.12. The average tensile strength values for the RSAM-24, RSAM-48 and RSAM-72 specimens are 52.16, 34.05 and 25.17 MPa, respectively, and the average elongation values are 2.2%, 0.6% and 0.8%, respectively. The observation is

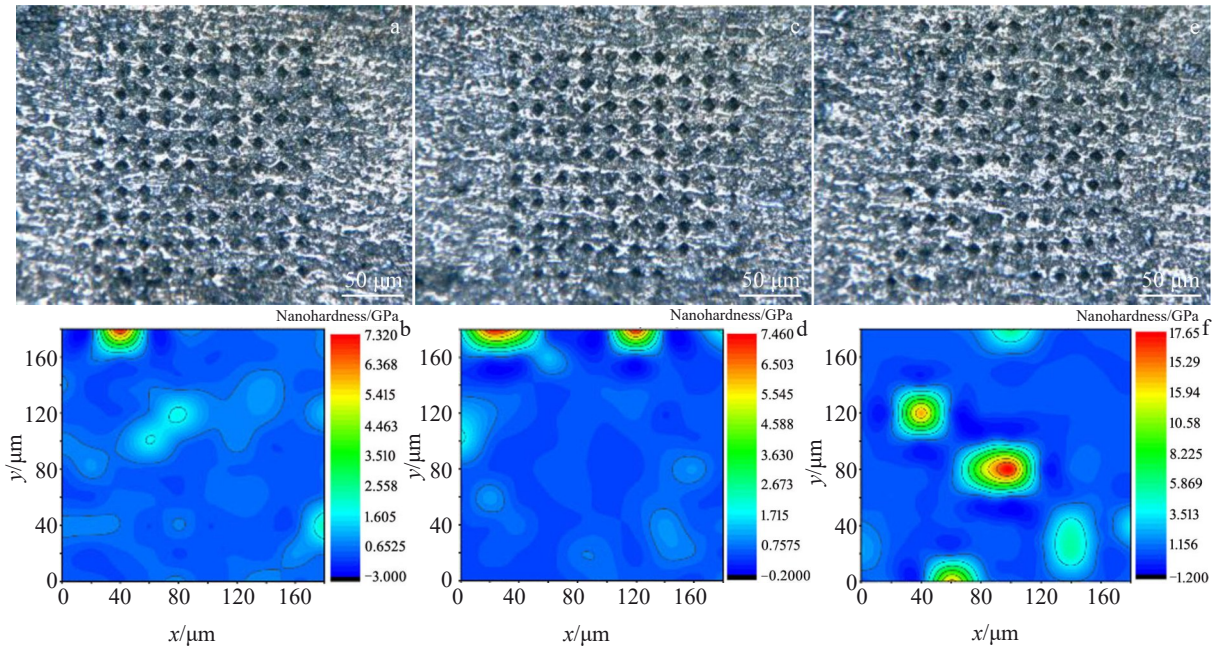


Fig.11 Microstructures of the corresponding region in Fig.3g (a, c, e); nanohardness distribution in the corresponding regions (b, d, f)

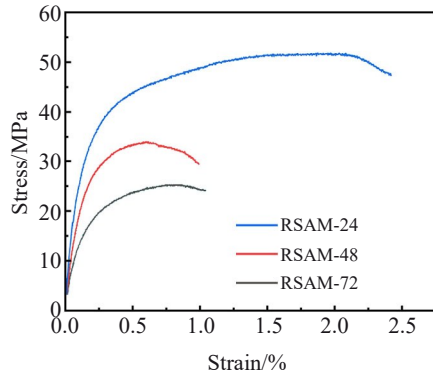


Fig.12 Engineering tensile stress-strain curves for different specimens

noteworthy that increase in tensile strength values is associated with the decrease in welding speeds. Compared with traditional powder bed fusion method^[35-36], the mechanical properties have not been significantly affected by the treatment.

The fractures consistently manifest at the interface layer in all specimens, underscoring an inadequate bonding performance between the additive layers, as shown in Fig. 13. However, many tough nests are observed on the fracture surface, indicating ductile fracture. The fracture mechanism

can be primarily attributed to the following three pathways. Firstly, interlayer cracking involves cracks that initiate within the interlayer bond, leading to the expansion of cracks along the interlayer bonding interface. The expansion leads to the separation of layers, resulting in subsequent material destabilization and fracture. The second kind of cracks mainly occurs at the interface between the Al matrix and SiCp. It is worth noting that the interface often shows defects such as voids, which leads to the formation of extended cracks. Lastly, the toughness of the Al matrix can also lead to cracking, causing material destabilization and subsequent fracture. There are many small pits at the fracture, which is due to the plastic mismatch between the Al matrix and the SiC, and cracks are generated around the SiCp. This means that the interface between Al matrix and SiC may have low resistance to dislocation movement and is prone to crack propagation under high tensile stress, so the fracture occurs in an intergranular mode with fine pits^[37]. Fig.14 shows a schematic diagram of the fracture mechanism. At the initial stage of axial stress loading, tiny cracks appear at the interlaminar bonding interface and pore defects. With the gradual increase in stress, cracks propagate along the surface of SiCp and the bonding interface between layers, leading to ductile cracking in the Al matrix. The cracks are expanded when the stress is further applied, ultimately leading to the fracture of the composite.

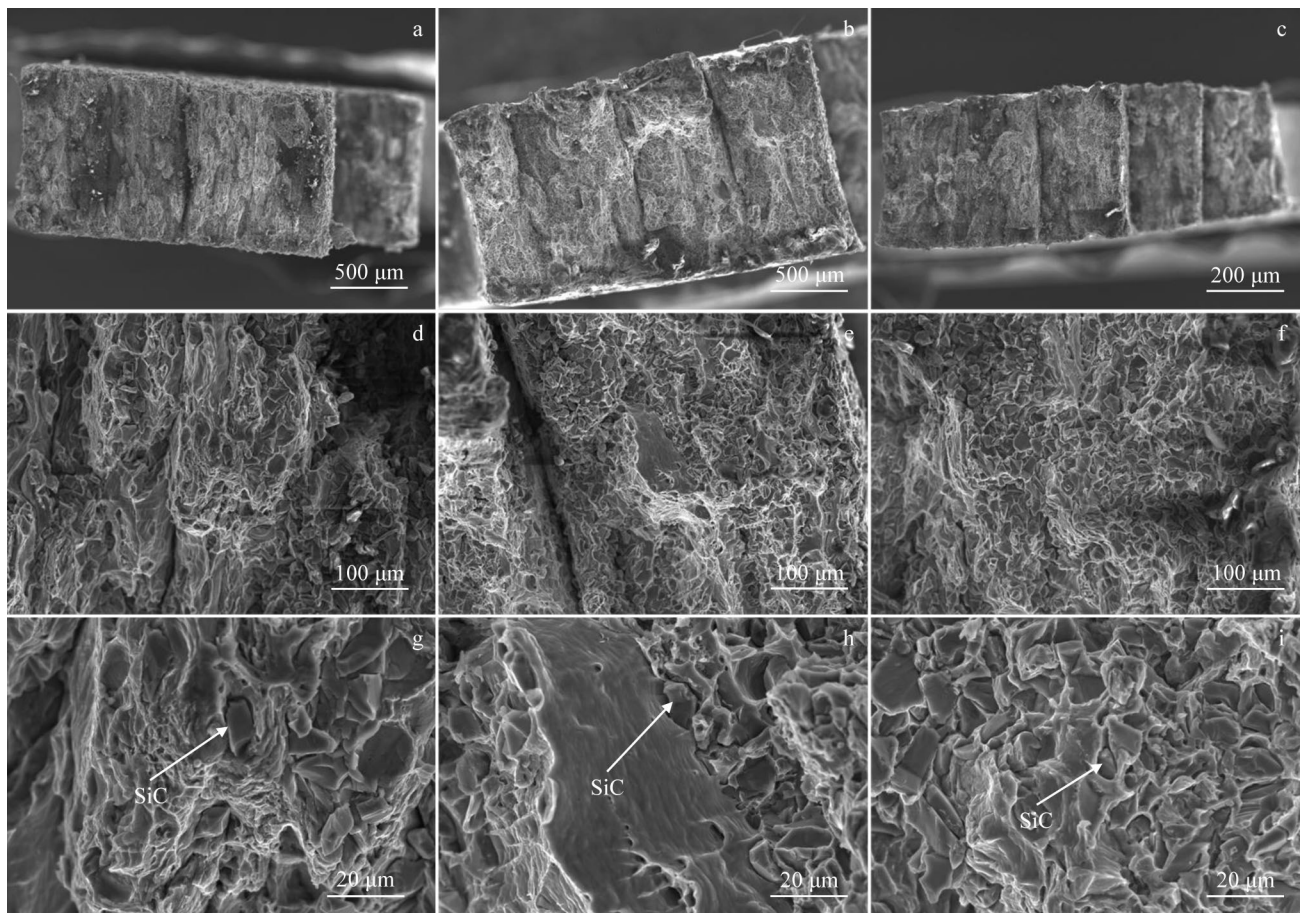


Fig.13 Fracture morphologies of RSAM-24 (a, d, g), RSAM-48 (b, e, h), and RSAM-72 (c, f, i) specimens

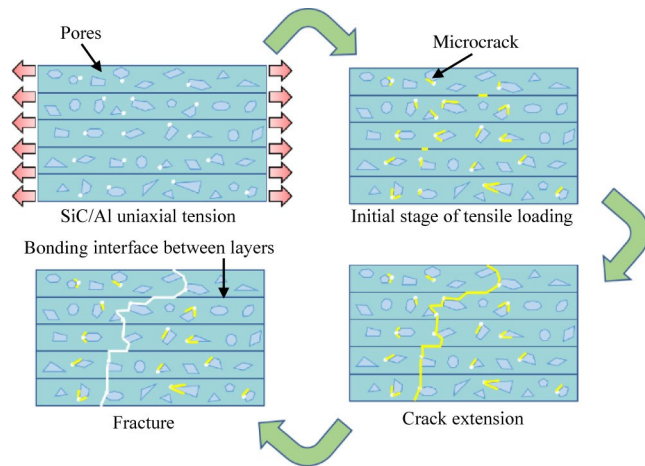


Fig.14 Schematic of fracture mechanism of SiCp/Al composites

3 Conclusions

1) The SiCp is uniformly distributed on the Al matrix, and there are some agglomerates and pore defects. The porosity increases with the increase in welding speed, and the microstructure of the RSAM-24 specimen exhibits the highest density of 2.706 g/cm^3 and a porosity of 1.672%.

2) Al 1060 particles melt locally after a large amount of instantaneous Joule heat is generated under the high contact resistance induced by pulsed current, and Al in the molten state fills the voids between SiC powders under the electrode pressure and capillarity, which finally promotes the formation of SiCp/Al composites.

3) The mechanical properties of the specimens decrease as the welding speed increases. Optimal mechanical properties are achieved when the welding speed is set at 24 cm/min. Specifically, the average hardness, tensile strength and elongation values are 463.736 MPa, 52.16 MPa and 2.2%, respectively.

References

- Altiparmak S C, Yardley V A, Shi Z et al. *International Journal of Lightweight Materials and Manufacture*[J], 2021, 4(2): 246
- Davis J R. *Aluminum and Aluminum Alloys*[M]. Ohio: ASM international,1993
- Xue Kemin, Wang Boxiaotian, Wu Guangshan et al. *Rare Metal Materials and Engineering*[J], 2021, 50(9): 3125
- Zhang Hao, Zhang Laichang, Liu Hongyu et al. *Virtual and Physical Prototyping*[J], 2023, 18(1): 16
- John C V, Abdel-Hamid M I, Muhammad S M et al. *Transactions of Nonferrous Metals Society of China*[J], 2021, 31(11): 3281
- Evans A, San Marchi C, Mortensen A et al. *Metal Matrix Composites*[M]. New York: Springer, 2003
- Qiu C, Su Y, Yang J et al. *Composites Part C: Open Access*[J], 2021, 4: 100120
- Wang M, Song B, Wei Q et al. *Journal of Alloys and Compounds*[J], 2019, 810: 151926
- Shen M J, Wang X J, Ying T et al. *Journal of Alloys and Compounds*[J], 2016, 686: 831
- Yang Zhigang, Zhao Zhijia, Yu Jianbo et al. *Rare Metal Materials and Engineering*[J], 2020, 49(2): 515 (in Chinese)
- Karabulut Y, Ünal R. *Journal of Materials Science*[J], 2022, 57(41): 19212
- Wang Xiaomin. *Rare Metal Materials and Engineering*[J], 2016, 45(7): 1714 (in Chinese)
- Mazahery A, Shabani M O. *Transactions of Nonferrous Metals Society of China*[J], 2012, 22(2): 275
- Hu Yong, Liu Fei, Wang Dahao et al. *Rare Metal Materials and Engineering*[J], 2021, 50(8): 2967
- Sun Y H, Xiong W H, Li C H. *Transactions of Nonferrous Metals Society of China*[J], 2010, 20(4): 624
- Samal P, Vundavilli P R, Meher A et al. *Journal of Manufacturing Processes*[J], 2020, 59: 131
- Reddy A P, Krishna P V, Rao R N. *Journal of Nanomaterials, Nanoengineering and Nanosystems*[J], 2017, 231(4): 155
- Wang Yunlei, Ren Liping, Yang Fangzhou et al. *Rare Metal Materials and Engineering*[J], 2022, 51(4): 1270
- Yuan Meini, Yang Yanqing, Huang Bin et al. *Rare Metal Materials and Engineering*[J], 2009, 38(8): 1321
- Xiao Bolu, Bi Jing, Zhao Mingjiu. *Metal Research*[J], 2002(9): 1006
- Bai C Y, Lan L, Xin R Y et al. *Fatigue*[J], 2022, 159: 106784
- Riquelme A, Rodrigo P, Escalera-Rodríguez M D et al. *Materials*[J], 2020, 13(15): 3331
- Zhang D, Yi D, Wu X et al. *Journal of Alloys and Compounds*[J], 2022, 894: 162365
- Xie H, Zhang J, Li F et al. *Ceramics International*[J], 2021, 47(21): 30826
- Astfálck L C, Kelly G K, Li X et al. *Advanced Engineering Materials*[J], 2017, 19(8): 1600835
- Astfálck Lachlan Connor, Kelly Gemma Kaye, Li Xiaopeng. *International Scholarly Research Notices*[J], 2012(10): 208760
- Zhao D, Yamaguchi T, Shu J et al. *Applied Surface Science*[J], 2020, 517: 145980
- Mira-Aguiar T, Galvão I, Leitão C et al. *Materiais 2015*[C]. Cambridge: Woodhead Publishing Limited, 2015: 21
- Wang W, Wang D, Yamaguchi T et al. *Surface and Coatings Technology*[J], 2017, 309: 136
- Ma H Y, Wang J C, Qin P et al. *Journal of Materials Science & Technology*[J], 2023, 183: 32
- Wang Jincheng, Zhu Rui, Liu Yujing et al. *Advanced Powder Materials*[J], 2023, 2(4): 100137
- Mhaske M S, Shirsat U M. *Materials Today: Proceedings*[J], 2021, 44: 376
- Riquelme A, Escalera-Rodríguez M D, Rodrigo P et al. *Journal of Alloys and Compounds*[J], 2017, 727: 671
- Viala J C, Fortier P, Bouix J. *Journal of Materials Science*[J],

- 1990, 25: 1842
- 35 Li Kunmao, Yang Junjie, Yi Yanliang et al. *Acta Materialia*[J], 2023, 256: 119112
- 36 Hooyar Attar, Matthias Bönisch, Mariana Calin et al. *Acta Materialia*[J], 2014, 76: 13
- 37 Wang Jincheng, Liu Yujing, Rabadia Chirag Dhirajlal et al. *Journal of Materials Science & Technology*[J], 2023, 61: 221

基于粉末堆积电阻增材制备 SiCp/Al 复合材料的组织与性能

王文琴¹, 陈吉根¹, 晏小松³, 韩召先⁴, 林刚², 陈杰²

(1. 南昌大学 先进制造学院, 江西 南昌 330031)

(2. 江西省检验检测认证总院 特种设备检验检测研究院, 江西 南昌 330029)

(3. 江西神州六合直升机有限责任公司, 江西 景德镇 333032)

(4. 江西昊宇重工有限公司, 江西 瑞金 341000)

摘要: 探讨了粉末填充电阻缝焊增材制造方法制备 SiCp/Al 复合材料。研究了焊接速度对试样显微组织和力学性能的影响, 揭示了单道多层沉积层的成形及断裂机理。结果表明: SiC 颗粒分布在 Al 基质上, 存在团聚和气孔缺陷。孔隙率随焊接速度的增加而升高, RSAM-24 试样组织最致密, 密度和孔隙率分别为 2.706 g/cm³ 和 1.672%。试样的力学性能随焊接速度的增加而降低, 焊接速度为 24 cm/min 时试样的力学性能最佳, 平均硬度、抗拉伸强度和延伸率分别为 463.736 MPa、52.16 MPa 和 2.2%。拉伸试样主要沿层间结合界面和 Al 基体与 SiC 颗粒结合界面处开裂, 断裂方式为韧性断裂。

关键词: 增材制造; 电阻缝焊; SiCp/Al; 硬度; 焊接速度

作者简介: 王文琴, 女, 1987年生, 博士, 副教授, 南昌大学先进制造学院, 江西 南昌 330031, E-mail: wangwenqin@ncu.edu.cn